QUANTUM PHYSICS

Mach-Zehnder interferometry using spin- and valley-polarized quantum Hall edge states in graphene

Di S. Wei,[1]* Toeno van der Sar,[2] Javier D. Sanchez-Yamagishi,[2,3] Kenji Watanabe,[4] Takashi Taniguchi,[4] Pablo Jarillo-Herrero,[3] Bertrand I. Halperin,[2] Amir Yacoby[1,2]

Confined to a two-dimensional plane, electrons in a strong magnetic field travel along the edge in one-dimensional quantum Hall channels that are protected against backscattering. These channels can be used as solid-state analogs of monochromatic beams of light, providing a unique platform for studying electron interference. Electron interferometry is regarded as one of the most promising routes for studying fractional and non-Abelian statistics and quantum entanglement via two-particle interference. However, creating an edge-channel interferometer in which electron-electron interactions play an important role requires a clean system and long phase coherence lengths. We realize electronic Mach-Zehnder interferometers with record visibilities of up to 98% using spin- and valley-polarized edge channels that copropagate along a pn junction in graphene. We find that interchannel scattering between same-spin edge channels along the physical graphene edge can be used to form beamsplitters, whereas the absence of interchannel scattering along gate-defined interfaces can be used to form isolated interferometer arms. Surprisingly, our interferometer is robust to dephasing effects at energies an order of magnitude larger than those observed in pioneering experiments on GaAs/AlGaAs quantum wells. Our results shed light on the nature of edge-channel equilibration and open up new possibilities for studying exotic electron statistics and quantum phenomena.

INTRODUCTION

Electron interference plays a central role in mesoscopic physics (*1*–*3*) and is regarded as one of the most promising routes for studying fractional and non-Abelian statistics (*4*, *5*) and quantum entanglement via two-particle interference (*6*, *7*). Quantum Hall edges form excellent building blocks for electron interferometers because they are single-mode channels that are protected from interchannel scattering by their quantum degrees of freedom, such as spin (*1*, *8*). Furthermore, they can be positioned via electrostatic gating and coupled at target locations that act as beamsplitters (*2*, *3*). The energy gaps between Landau levels (LLs) allow for the creation of interferometers and quantum point contacts even in materials that do not have a zero-field bandgap, such as graphene (*9*, *10*). Graphene may provide an advantage compared to conventional GaAs edge-channel interferometers (*11*–*14*) because the absence of a bandgap allows the creation of hole- and electron-like edge channels that naturally meet, copropagate, and separate at gate-defined pn interfaces (*15*, *16*). The additional valley degree of freedom and the associated unique nature of graphene quantum Hall states (*17*, *18*) open up new opportunities for addressing long-sought goals of electron interferometry, such as the observation of non-Abelian statistics (*19*). In addition, the valley isospin provides new possibilities for controlling interchannel scattering (*20*), a requirement for creating edge-channel interferometers. However, although graphene pn junctions in the quantum Hall regime have been studied extensively (*8*, *15*, *16*, *21*–*26*), creating an edge-channel interferometer using spin- and valley-polarized edge channels has remained an outstanding challenge.

In the paradigmatic electronic interferometer—the Mach-Zehnder interferometer (MZI)—a beam of electrons is split into two paths by a beamsplitter and recombined at a second beamsplitter (*3*). Here, we engineer MZIs consisting of same-spin, opposite-valley quantum Hall edge channels that copropagate along a pn junction in graphene. Using magnetic and trans-junction electric fields, we can tune into a regime in which either one or both pairs of the same-spin edge channels belonging to the zeroth LL (zLL) form MZIs that coherently mediate the cross-junction transport (Fig. 1A). We find that these channels can be well isolated from those belonging to other LLs, enabling us to study a target interferometer over a large range of electric fields and tune into regimes with visibilities as high as 98%. By studying pn interfaces of different lengths, we show that the interferometer beamsplitters are located where the pn interface meets the physical graphene edges, which we attribute to strong intervalley scattering at the physical graphene edge and the absence of intervalley scattering along the gate-defined edge. We independently verify this conclusion using a device wherein we can tune the number of edge channels copropagating along either a physical or gate-defined edge.

RESULTS

Constructing an MZI in a graphene pn junction

To construct an MZI of spin- and valley-polarized edge channels, we use a hexagonal boron nitride (hBN)–encapsulated monolayer of graphene (see Fig. 1B and Methods). We tune into the quantum Hall regime using a perpendicular magnetic field B and define two regions of different charge densities n_T and n_B using a bottom gate that affects both n_T and n_B and a top gate that affects only n_T (Fig. 1B). The number of edge channels in these regions is given by the filling factors $\nu_{T,B} = \frac{h}{eB} n_{T,B}$, where e is the electron charge, and h is Planck's constant. The observation of integer quantum Hall steps in a measurement of the two-terminal conductance at $B = 4$ T in the regime where $\nu_T > 0$ and $\nu_B > 0$ confirms that the spin and valley degeneracy is lifted (fig. S1).

Next, we create a pn junction by tuning into the regime where $\nu_T < 0$ and $\nu_B > 0$ and study which edge channels mediate charge transport across the junction. When we measure the conductance g as a function of ν_T and ν_B at $B = 4$ T (Methods), we observe four regions with distinct

[1]John A. Paulson School of Engineering and Applied Sciences, Harvard University, Cambridge, MA 02138, USA. [2]Department of Physics, Harvard University, Cambridge, MA 02138, USA. [3]Department of Physics, Massachusetts Institute of Technology, Cambridge, MA 02139, USA. [4]Advanced Materials Laboratory, National Institute for Materials Science, Tsukuba, Ibaraki 305-0044, Japan.
*Corresponding author. Email: diwei@fas.harvard.edu

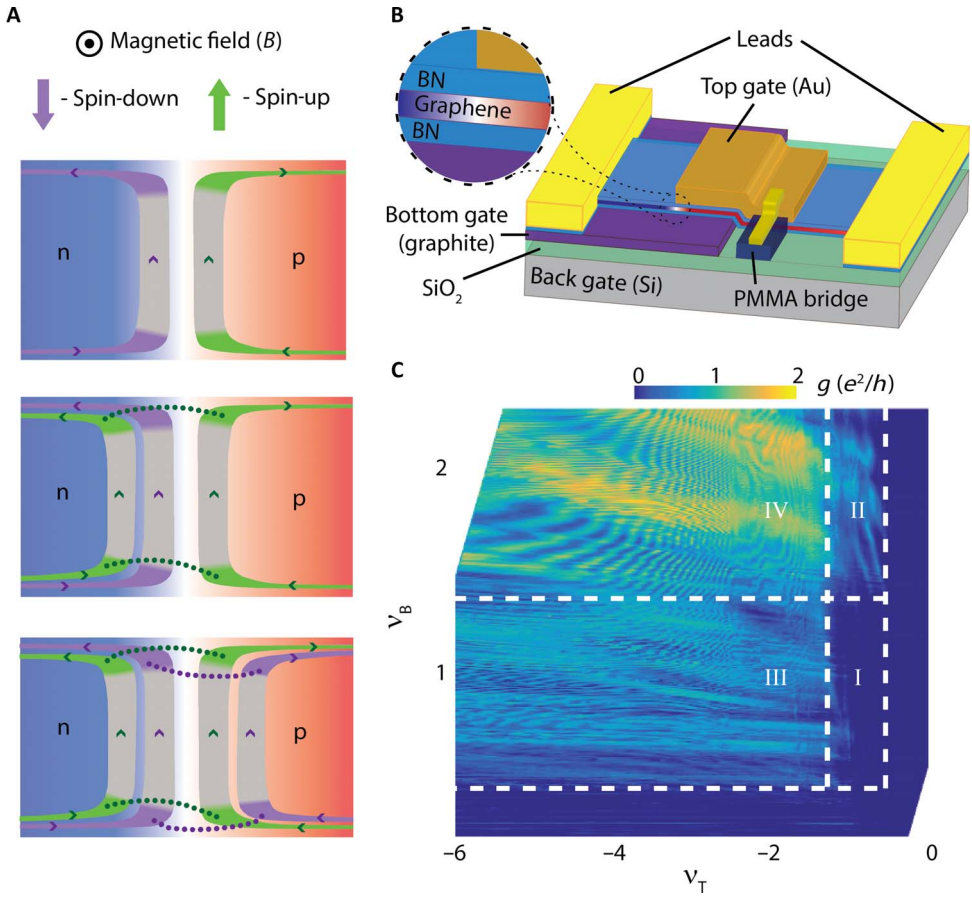

Fig. 1. Creating an MZI using spin- and valley-polarized quantum Hall edge channels. (**A**) Schematic illustration of the formation of MZIs at a graphene pn junction. Green and purple denote quantum Hall edge channels of opposite spin. Top panel: At (ν_B, ν_T) = (1, − 1), where ν_B (ν_T) is the filling factor in the n-region (p-region); two edge channels run along the interface. Their opposite spin suppresses interchannel scattering. Middle panel: At (ν_B, ν_T) = (2, − 1), a pair of spin-up edge channels forms an MZI. Interchannel scattering occurs at the ends of the junction, as indicated by dotted lines. Bottom panel: At (ν_B, ν_T) = (2, − 2), two pairs of same-spin edge channels form two MZIs. (**B**) Device 1: An edge-contacted monolayer graphene flake encapsulated in hBN. The top gate (Au) and bottom gate (graphite) define the pn junction (p, red color; n, blue color). The top hBN dielectric is 20-nm thick and the bottom is 30-nm thick. The top gate is contacted by a lead that runs over a bridge fabricated from hard-baked PMMA to avoid shorting to the graphene flake. The back gate (Si) is used to strongly increase the p-doping of the graphene leading up to the right lead and to reduce the contact resistance. The SiO_2 back-gate dielectric is 285-nm thick. (**C**) Two-terminal conductance of device 1 in the pn regime at B = 4 T. We distinguish four regions (dashed boxes). Region I corresponds to ν_B = 1 and ν_T = −1. Region II corresponds to ν_T = − 1 and $\nu_B \geq 2$. Region III corresponds to ν_B = 1 $\nu_T \leq -2$. Region IV corresponds to $\nu_B \geq 2$ and $\nu_T \leq -2$.

ranges of conductance values and the first indications of conductance oscillations (Fig. 1C). In region I, the conductance of the junction is near zero, which we attribute to the situation depicted in the top panel of Fig. 1A (where $\nu_B = 1$ and $\nu_T = -1$). Here, one n-type spin-down and one p-type spin-up edge channel copropagate along the junction. Because these channels have opposite spins, interchannel scattering is suppressed (*8*). When we cross from region I into region II, we begin to observe transport across the junction. We attribute this to an additional spin-up edge channel having entered on the n-side (so that $\nu_B = 2$ and $\nu_T = -1$); electrons in this channel can scatter into the spin-up channel on the p-side (see middle panel in Fig. 1A). In this process, the spin-up electron crosses the intermediate spin-down edge channel. We presume that tunneling into this edge channel is essentially zero because of the opposite spin (*8*). The observed conductance ranges approximately between 0 and e^2/h, consistent with one pair of edge channels mediating transport across the junction. Similarly, in region III, we obtain the situation in which $\nu_B = 1$ and $\nu_T = -2$, and we attribute the observed conductance to scattering between the two spin-down edge channels. Markedly, in region III, the conductance does not change notably when we keep adding edge channels on the p-side (going to $\nu_B = 1$ and $\nu_T < -2$). We conclude that these additional channels do not contribute to the trans-junction conductance, presumably because they belong to a higher LL, which makes them spatially too distant from the pn interface, which has also been seen in the study of Klimov *et al.* (*26*). Crossing into region IV ($\nu_B \geq 2$ and $\nu_T \leq -2$), we observe that the average conductance increases and ranges between 0 and $2e^2/h$. We attribute this to two pairs of same-spin edge channels mediating transport across the junction. Again, we see no sign of edge channels belonging to higher LLs entering the system and contributing to the trans-junction conductance. We conclude that the edge channels belonging to the zLL mediate the trans-junction conductance, well isolated from edge channels belonging to higher LLs.

The relative isolation of the edge channels that belong to the zLL allows us to study a target pair of edge channels over a large range

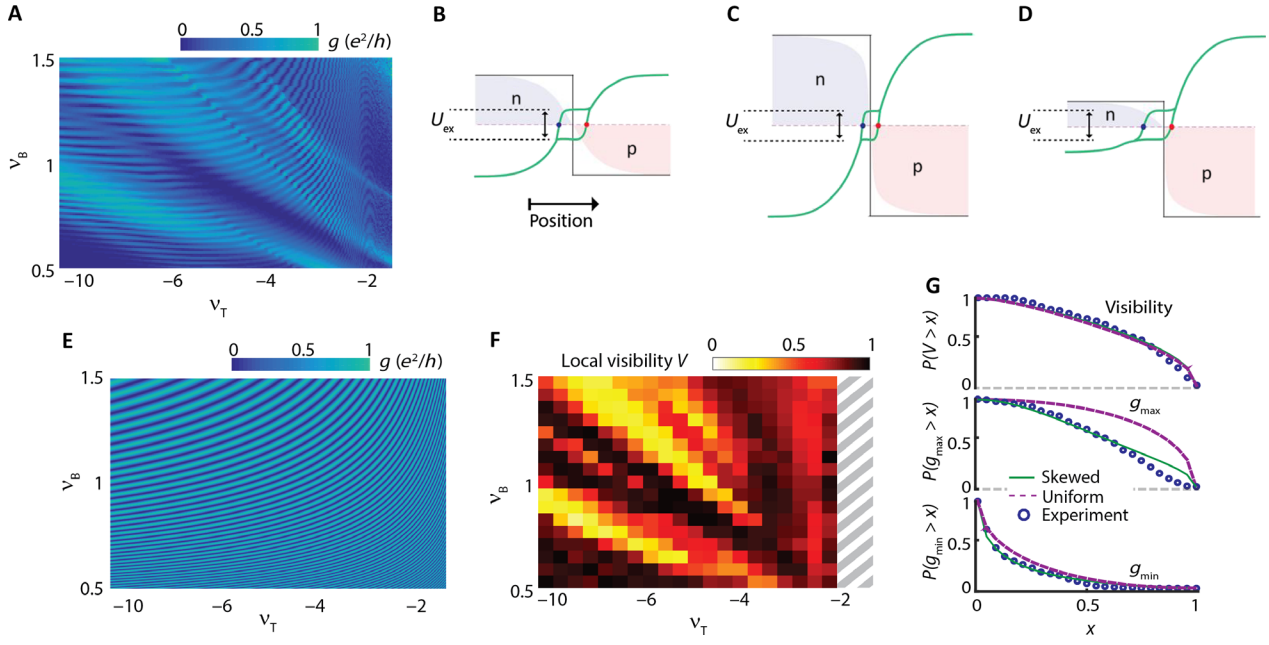

Fig. 2. Characterization of a single MZI. (**A**) Two-terminal conductance of device 1 at $B = 9$ T, over a range of filling factors corresponding to a single interferometer at the pn junction. (**B**) Modeling the charge-density dependence of the distance between the edge channels that form an MZI. The red and blue shading illustrates the spatial variation of the charge density close to the pn junction. The green line illustrates the spatial variation of the energies of the exchange-split $\nu = 1$ and $\nu = -2$ Landau sublevels. The edge channels are located at the positions where these sublevels intersect the Fermi energy. The distance between the edge channels determines the flux through the interferometer. Far from the pn junction, where the lowest LL is completely empty ($\nu = -2$) or completely full ($\nu = 2$), the exchange-splitting U_{ex} vanishes. However, near the pn junction, the electronic ground state can develop an imbalance in the valley occupation, leading self-consistently to a nonzero U_{ex}. (**C**) Increasing the electron and hole densities decreases the distance between the edge channels. (**D**) A strong imbalance between the electron and hole densities. (**E**) Simulation of the two-terminal conductance as a function of filling factors based on the model sketched in (B) to (D). (**F**) Local visibility of the conductance oscillations observed in (A). The gray dashed box indicates where the visibility was not extracted because of nonresolved oscillations. (**G**) Blue circles: Experimentally determined probability of finding a visibility, g_{max}, or g_{min} greater than x. Visibility is extracted from the color plot in (F); g_{min} and g_{max} are extracted from the color plots in fig. S3 (A and B). Purple dashed line: The theoretical prediction based on MZIs with beamsplitters described by random scattering matrices that correspond to beamsplitter transmission probabilities uniformly distributed between 0 and 1. Green solid line: The theoretical prediction based on MZIs with beamsplitters described by a skewed distribution of transmission probabilities (fig. S3C and note S2).

of filling factors. As we increase the magnetic field to $B = 9$ T and concentrate on region III, wherein $\nu_B = 1$ and $\nu_T \leq -2$, we observe a striking pattern of conductance oscillations (Fig. 2A) whose key features, such as shape and periodicity, depend on both ν_B and ν_T. These oscillations cannot be explained by semiclassical snake states or similar low-field phenomena, which have been invoked to explain oscillations observed at lower magnetic fields (*27*–*30*). A semiclassical description is valid when multiple LLs are occupied, and the cyclotron radius is large compared to the magnetic length. In our case, we are working in the extreme quantum limit, where the participating electrons are entirely in the zLL. We argue below that the oscillations we see in this case result from interference between two parallel edge channels, corresponding to different valley configurations, whose separation in momentum and space is a consequence of the Coulomb exchange interaction. Therefore, the period of the oscillations along the length of the junction is controlled by these interaction effects, in contrast with the case of snake states, where the period is determined by the sum of the cyclotron radii on the two sides of the junction. As we will further argue below, the well-defined periodicity of these oscillations indicates that scattering between the two edge channels that mediate the cross-junction transport occurs at only two points along the junction. These points form the beamsplitters that define our MZI. Its conductance, in units of e^2/h, is given by

$$g = |r_1 t_2|^2 + |r_2 t_1|^2 + 2|r_1 t_2 r_2 t_1| \cos(\varphi + \varphi_0)$$

where t_i (r_i) is the transmission (reflection) amplitude of the ith beamsplitter, with $|r_i|^2 + |t_i|^2 = 1$. The phase $\varphi = 2\pi \frac{BA}{\Phi_0}$ arises from the Aharonov-Bohm effect, where $\Phi_0 = h/e$ is the flux quantum, A is the effective area enclosed by the two edge channels, and φ_0 is an unknown phase associated with the beamsplitters.

Because the measurement in Fig. 2A is performed at a fixed magnetic field, we attribute the conductance oscillations to a changing distance between the two edge channels and a resulting changing flux through the interferometer. We can analyze the charge density–dependent locations of these channels by determining where the two corresponding exchange-split Landau sublevels cross the Fermi energy using a simple model for the spatial dependence of the sublevel energy (Fig. 2, B to D, and note S1). This model indicates that as the charge densities increase (from Fig. 2, B and C), the edge-channel separation decreases. Furthermore, when the charge density is small (large) on a particular side of the junction, the edge-channel separation is relatively sensitive (insensitive) to the charge density on that side of the junction (Fig. 2D). Figure 2E shows that this model reproduces the key features of the data in Fig. 2A. Further data in the $\nu_B \geq 2$ and $\nu_T \leq -2$ regime, wherein two MZIs act simultaneously (as depicted in the bottom panel of Fig. 1A), are shown in fig. S2.

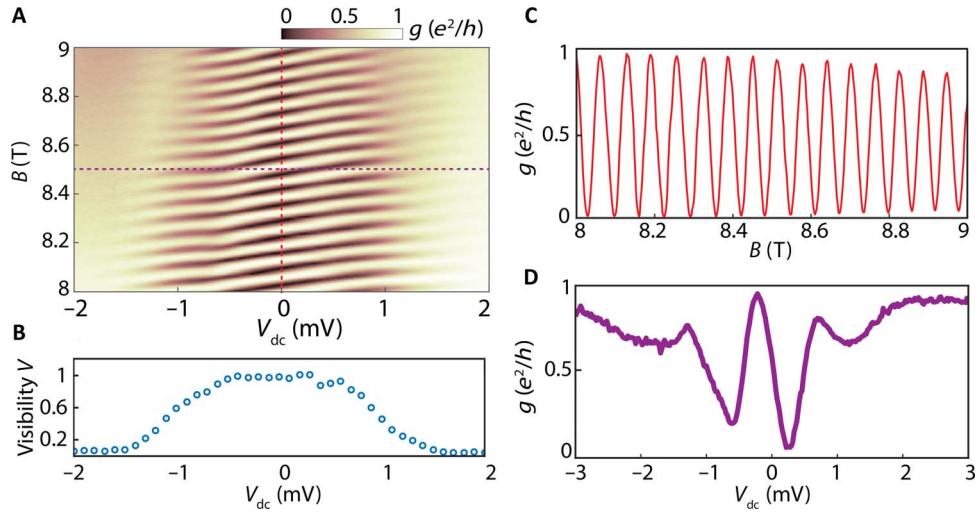

Fig. 3. Mach-Zehnder oscillations as a function of magnetic field and dc voltage bias. (**A**) Two-terminal differential conductance as a function of magnetic field B and dc voltage bias V_{dc} at $(\nu_B, \nu_T) = (1, -2)$, for which only one interferometer is formed at the pn interface. (**B**) Visibility of the conductance oscillations shown in (A) as a function of dc bias. (**C**) Conductance oscillations with B at zero dc bias corresponding to the red dotted line in (A). From the period $\Delta B = 66$ mT, we calculate the distance between edge states to be 52 nm, assuming that the distance between the beamsplitters is given by the 1.2-μm width of the device. (**D**) Line trace corresponding to the purple dotted line in (A) showing oscillations with respect to V_{dc}.

Beamsplitter characteristics

The visibility of the oscillations in an MZI depends on the phase coherence and the transmission characteristics of the beamsplitters. We analyze the range of visibilities observed in the measurement shown in Fig. 2A by dividing the measurement range into a grid and calculating the local visibility $V = (g_{max} - g_{min})/(g_{max} + g_{min})$, where g_{max} and g_{min} are the maximum and minimum conductance, respectively, within each block (Fig. 2F and fig. S3, A and B). In Fig. 2G, we plot the resulting experimental cumulative probability distribution function that indicates the probability of finding a visibility, g_{min}, or g_{max} greater than x. We compare these distributions to a theoretical prediction that is based on the assumption that the incoming and outgoing channels of each of the two beamsplitters of the MZI are connected by random U(2) matrices in valley space (note S2). This comparison indicates that in the measurement of Fig. 2A, the beamsplitter transmission probabilities are not perfectly uniformly distributed between 0 and 1 (Fig. 2G) but are instead somewhat skewed toward lower trans-junction conductance (fig. S3C and note S2). Remarkably, in several regions of the conductance map (Fig. 2A), we find visibilities as high as 98%, indicating a near-perfect phase coherence along the pn interface. In addition, in some regions, the conductance oscillates nearly between 0 and e^2/h, indicating nearly 50/50 beamsplitters. Further insight into beamsplitter transmission probabilities yielding a particular Mach-Zehnder visibility can be gained from fig. S3 (D and E).

Dependence of the Mach-Zehnder interference on magnetic field and dc voltage bias

Next, we tune to a region of high visibility and study the conductance as a function of B and a dc voltage bias V_{dc} (Fig. 3A). We observe that the visibility stays near-unity for $|V_{dc}| < 0.5$ mV (Fig. 3B) and decreases at larger $|V_{dc}|$, which may be due to thermal averaging or electron-electron interactions (*3*, *14*). For the field range of 8 to 9 T in Fig. 3C, measurements at $V_{dc} = 0$ show a constant oscillation period ΔB, which is consistent with an assumption that the area enclosed by the interferometer is constant and given by $A = \frac{\Phi_0}{\Delta B}$. Subject to this assumption, we determine an edge-channel separation of 52 nm. Oscillations with V_{dc} are also observed (Fig. 3D), indicating a bias-dependent edge-channel separation, which may be a result of a bias-induced electrostatic gating effect (*14*). Note that at larger filling factors, we see multiple frequencies, changing frequency with field, and lobe structures, which have previously been attributed to Coulomb interactions in GaAs devices (fig. S4) (*12*–*14*). We leave the analysis of these effects to a future study.

Varying the length of the pn interface

To confirm that the beamsplitters are located where the pn interface meets the physical graphene edges, we measure the MZI oscillation frequency as a function of the interface length. We use device 2 (Fig. 4, A and B) that has five top gates (TG1 to TG5) of varying lengths that we can address individually in two-terminal conductance measurements by using the appropriate leads. Using top and bottom gates to control the filling factors in the top-gated and non–top-gated regions, ν_T and ν_B, respectively, we can tune into a regime where $\nu_T < 0$ and $\nu_B > 0$ to create an npn configuration with two pn junctions in series (fig. S5). When we measure the two-terminal conductance at $B = 8$ T as a function of ν_T and ν_B (Fig. 4C and fig. S5), we recognize the regions corresponding to zero, one, and two pairs of same-spin edge channels mediating transport across the pn junctions, as discussed above for the measurement in Fig. 1C and further analyzed in note S3. In addition, we observe clear conductance oscillations, of which we expect the frequencies to reflect the gate lengths. To analyze these frequencies, we focus on the limit $|\nu_{B,T}| \gg 1$ in which the edge-channel separation and the associated Aharanov-Bohm flux are expected to vary as $\sim 1/(\sqrt{\nu_B} + \sqrt{-\nu_T})$ (note S4). We plot the conductance data against $1/(\sqrt{\nu_B} + \sqrt{-\nu_T})$ and use a Fourier transform to determine the frequency spectrum (fig. S6). Normalizing the frequency axis to the average length of TG5, we find peaks at locations that correspond reasonably well to those expected on the basis of the lengths of the different gates (Fig. 4D). We conclude that the beamsplitters are located where the pn interfaces meet the

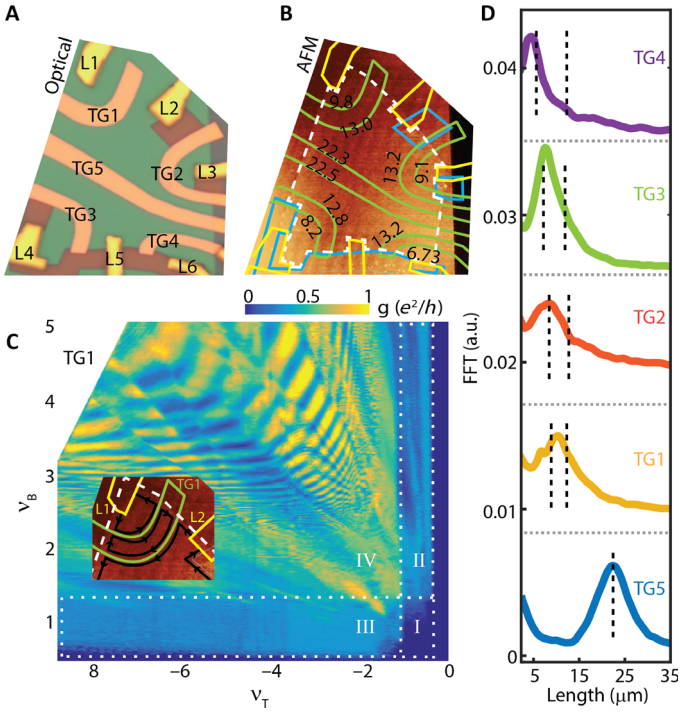

Fig. 4. Gate-length dependence of the Mach-Zehnder oscillations. (**A**) Optical microscopy image of device 2: An edge-contacted, hBN-encapsulated monolayer of graphene with five top gates of different lengths. The top-gate dielectric (hBN) is 17-nm thick. The bottom hBN layer is 16-nm thick. The back-gate dielectric (SiO_2) is 285-nm thick. Leads (L1 to L6) are yellow. Top gates (TG1 to TG5) are orange. Using the top and back gate, we induce an npn charge configuration with two pn junctions and their associated MZIs connected in series. (**B**) Atomic force microscopy (AFM) image of device 2. The graphene is indicated by the white dashed line. Top gates are outlined in green, leads are in yellow, and etched regions are in blue. The lengths of both sides of each top gate are indicated in micrometers. (**C**) Two-terminal conductance measured across top gate 1 (TG1) using leads L1 and L2 at $B = 8$ T. Region I corresponds to $\nu_B = -1$ and $\nu_T = 1$. Region II corresponds to $\nu_T = -1$ and $\nu_B \geq 2$. Region III corresponds to $\nu_T \leq -2$ and $\nu_B = 1$. Region IV corresponds to $\nu_B \geq 2$ and $\nu_T \leq -2$. Inset: Close-up of (B) showing the top gate and the two leads used in this measurement. The edge channels are indicated by black lines. (**D**) Frequency spectrum (FFT, fast Fourier transform) of the conductance oscillations for all top gates. The *x* axis is normalized to the approximate length of TG5. The expected frequencies for each gate are indicated by the black dashed lines.

physical graphene edge. Remarkably, it follows that each oscillation corresponds to a minute change in the edge-channel separation; for example, for the gate length of device 1 ($L = 1.2$ μm), this change equals $\frac{\Phi_0}{BL} = 3.7$ Å.

Edge-channel equilibration along gate-defined and physical edges

Finally, we demonstrate the absence of interchannel scattering along a gate-defined edge and the full equilibration of same-spin edge channels running along a physical edge. We use device 3 (Fig. 5, A to D), which has two top gates that determine the number of edge channels running from the left to the right lead, and a top gate (referred to as the side gate) that determines which fraction of the edge channels in the central region travels along the lower physical edge instead of along the side-gate–defined edge. We first confirm the presence of robust broken symmetry quantum Hall states (fig. S7C). We then apply a bias V_{IN} between the left and top lead and measure the potential at the right lead (V_{OUT}) as a function of the side-gate filling factor (Fig. 5E). The edge-channel equilibration in the central region should reduce the chemical potential at the right lead below that of the input lead. The precise match between data and model (described in note S5) in Fig. 5E demonstrates that edge channels do not equilibrate along the side-gate–defined edge, although they do equilibrate along the physical edge provided that they have the same spin. Note that we observe no MZI oscillations as we sweep the magnetic field between 8.9 and 9 T (fig. S7, D to F), presumably because there are no locations acting as beamsplitters, because the edge channels do not meet at a physical edge before and after copropagating along a gate-defined edge.

DISCUSSION

The experiments presented here demonstrate a robust method of engineering a high-visibility MZI in a graphene quantum Hall system by harnessing edge channels copropagating along a pn junction. Although previous measurements on graphene pn junctions in the quantum Hall regime showed results ranging from full equilibration between edge channels copropagating along the pn junction (with no noticeable interference effects) (*16*) to a complete absence of trans–pn junction conductance (*8*), we believe we observe interference between the copropagating channels belonging to the zLL because we have (i) a low-disorder device in which the Landau level degeneracy is fully lifted and in which dephasing is sufficiently low and (ii) we use a top gate that is relatively close to the graphene [closer than the top gate used in the study of Amet *et al.* (*8*)] so that the electrical potential profile across the pn junction is sharp and allows the edge states to come close enough to each other to be coupled and form beamsplitters. This opens up the possibility of a variety of interferometry experiments and grants us the diagnostic capabilities of measuring subnanometer shifts in edge-channel separation. Here, we observe transport across the insulating $\nu = 0$ state, which is expected to be in a canted antiferromagnetic (CAF) phase in bulk graphene (*31*, *32*). The fact that we find that spin polarization is well preserved in our samples suggests that the CAF phase may be suppressed in a narrow pn junction in favor of a state where spins are fully polarized along the direction of the magnetic field.

METHODS

Sample fabrication

All devices were fabricated on doped Si chips with a 285-nm layer of SiO_2 that acted as a dielectric for the Si back gate. Graphene was mechanically exfoliated from bulk graphite obtained from NGS Naturgraphit GmbH using 1009R tape from Ultron Systems and subsequently encapsulated in hBN using a dry transfer process (*33*). For device 1, we placed the resulting stack on a graphite bottom gate. Before the first metal deposition step, we annealed the devices in vacuum at 500°C to improve device quality. Then, we created top gates using electron-beam lithography and thermal evaporation of Cr/Au. To fabricate edge contacts to the graphene in device 1 without shorting to the graphite bottom gate, we selectively etched the stack down such that the bottom hBN flake remained and protected the graphite while simultaneously exposing the graphene flake. To fabricate the edge contacts to the graphene in devices 2 and 3, we etched through the entire hBN/graphene stack. We then created edge contacts by thermally evaporating Cr/Au while rotating the sample using a tilted rotation stage. Finally, we etched

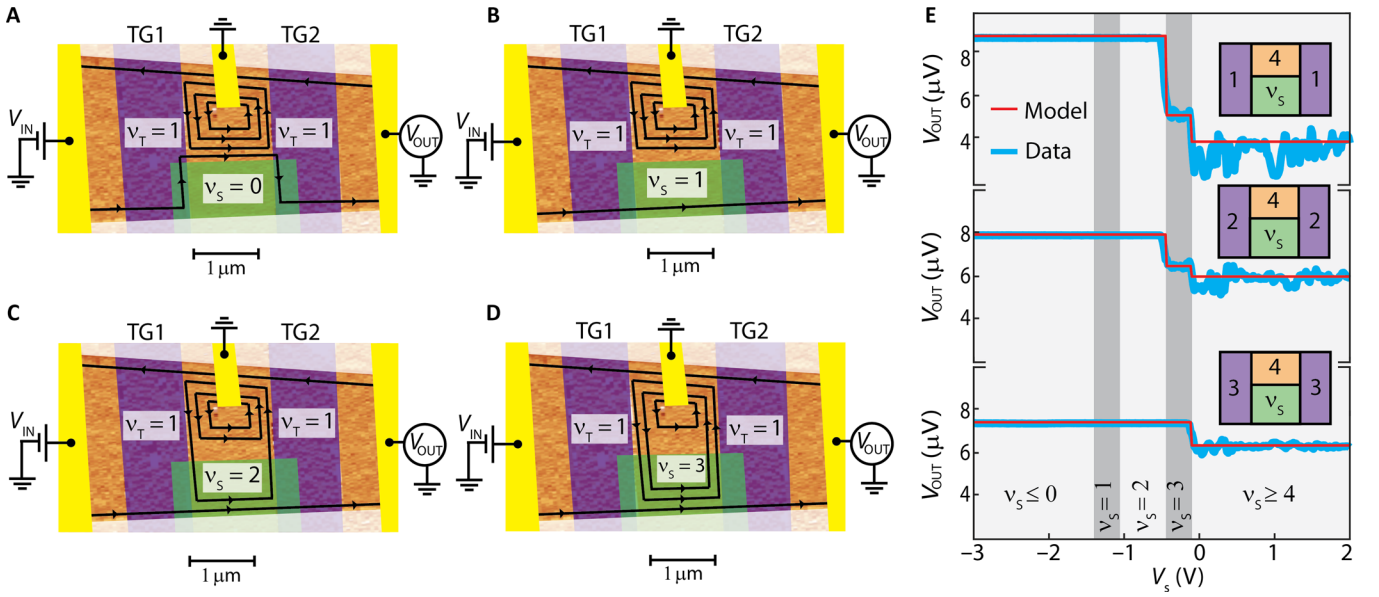

Fig. 5. Absence of equilibration between edge channels running along a gate-defined edge. (**A** to **D**) Schematic of device 3: An edge-contacted, hBN-encapsulated monolayer of graphene with two top gates and a side gate. An AFM image shows the top gates (TG1 and TG2, false-colored purple) on top of the hBN-encapsulated graphene flake. Yellow (green) indicates the leads (side gate). The progression of (A) to (D) illustrates the changing locations of the edge channels in the central region as the filling factor under the side gate is tuned from $\nu_S = 0$ to $\nu_S = 3$, whereas the regions under TG1 and TG2 are kept at $\nu_T = 1$, and the rest of the device is kept at $\nu_B = 4$. The circulating edge states near the contacts are omitted for clarity. (**E**) Voltage measured at the right contact as a function of the side-gate voltage V_S that tunes the side-gate filling factor ν_S for $\nu_T = 1$, 2, and 3, as indicated by the insets. The data (blue) is an average of a set of traces taken at different magnetic fields between 7.9 and 8 T (fig. S7). The red line indicates the expected values given by a model that assumes no equilibration along the gate-defined edge and full equilibration between same-spin channels along the physical edge, taking into account the independently measured contact resistances (note S5). The top trace corresponds to the sequence depicted in (**A** to **D**).

the devices into the desired geometry by reactive ion etching in O_2/CHF_3 using a poly(methyl methacrylate) (PMMA)/HSQ bilayer of resist (patterned by electron-beam lithography) as the etch mask.

Measurement

Our measurements were performed in a Leiden dry dilution refrigerator with a base temperature of 20 mK. Measurements of differential conductance were performed using a lock-in amplifier with an ac excitation voltage of 10 μV at 17.77 Hz. All measurements of differential conductance were corrected for contact/line resistances, which were independently determined by lining up the robust $\nu = 2$ quantum Hall conductance plateau with $2e^2/h$. We estimated all filling factors based on a parallel-plate capacitor model with a correction to account for the quantum capacitance (note S6).

SUPPLEMENTARY MATERIALS

Supplementary material for this article is available at http://advances.sciencemag.org/cgi/content/full/3/8/e1700600/DC1

fig. S1. Characterization of device 1 in the regime where $\nu_B > 0$ and $\nu_T > 0$ (which we call the nn′ regime).
fig. S2. Two-terminal conductance of device 1 in the pn regime (in which $\nu_B > 0$ and $\nu_T < 0$) at $B = 4$ T and large filling factors.
fig. S3. Analysis of transmission and reflection in Mach-Zehnder beamsplitters.
fig. S4. The effect of a dc bias on the differential conductance of a pn junction.
fig. S5. Analyzing the average conductance observed in npn measurements on device 2.
fig. S6. Analyzing the gate-length dependence of the Mach-Zehnder oscillation frequencies observed in npn devices.
fig. S7. Device 3: verifying the presence of broken symmetry quantum Hall states and measurements of edge channel equilibration as a function of magnetic field.
note S1. Modeling the distance between the edge channels forming an MZI.
note S2. Scattering model for an MZI at a graphene pn junction.
note S3. Conductance of two MZIs in series.
note S4. Analyzing the gate-length dependence of the Mach-Zehnder oscillation frequencies observed in the npn measurements on device 2.
note S5. Gate-defined equilibration studies.
note S6. Calculating charge densities and filling factors from gate voltages.
References (*34*, *35*)

REFERENCES AND NOTES

1. S. Datta, *Electronic Transport in Mesoscopic Systems* (Cambridge Univ., 1995).
2. C. d. C. Chamon, D. E. Freed, S. A. Kivelson, S. L. Sondhi, X. G. Wen, Two point-contact interferometer for quantum Hall systems. *Phys. Rev. B* **55**, 2331–2343 (1997).
3. Y. Ji, Y. Chung, D. Sprinzak, M. Heiblum, D. Mahalu, H. Shtrikman, An electronic Mach-Zehnder interferometer. *Nature* **422**, 415–418 (2003).
4. K. T. Law, D. E. Feldman, Y. Gefen, Electronic Mach-Zehnder interferometer as a tool to probe fractional statistics. *Phys. Rev. B* **74**, 045319 (2006).
5. D. E. Feldman, A. Kitaev, Detecting non-Abelian statistics with an electronic Mach-Zehnder interferometer. *Phys. Rev. Lett.* **97**, 186803 (2006).
6. P. Samuelsson, E. V. Sukhorukov, M. Büttiker, Two-particle Aharonov-Bohm effect and entanglement in the electronic Hanbury Brown-Twiss setup. *Phys. Rev. Lett.* **92**, 026805 (2004).
7. B. Yurke, D. Stoler, Bell's-inequality experiments using independent-particle sources. *Phys. Rev. A* **46**, 2229–2234 (1992).
8. F. Amet, J. R. Williams, K. Watanabe, T. Taniguchi, D. Goldhaber-Gordon, Selective equilibration of spin-polarized quantum Hall edge states in graphene. *Phys. Rev. Lett.* **112**, 196601 (2014).
9. S. Nakaharai, J. R. Williams, C. M. Marcus, Gate-defined graphene quantum point contact in the quantum hall regime. *Phys. Rev. Lett.* **107**, 036602 (2011).
10. K. Zimmerman, A. Jordan, F. Gay, K. Watanabe T. Taniguchi, Z. Han, V. Bouchiat, H. Sellier, B. Sacépé, Tunable transmission of quantum Hall edge channels with full degeneracy lifting in split-gated graphene devices. *Nat. Commun.* **8**, 14983 (2017).
11. I. Neder, N. Ofek, Y. Chung, M. Heiblum, D. Mahalu, V. Umansky, Interference between two indistinguishable electrons from independent sources. *Nature* **448**, 333–337 (2007).
12. I. Neder, M. Heiblum, Y. Levinson, D. Mahalu, V. Umansky, Unexpected behavior in a two-path electron interferometer. *Phys. Rev. Lett.* **96**, 016804 (2006).

13. P. Roulleau, F. Portier, D. C. Glattli, P. Roche, A. Cavanna, U. Gennser, D. Mailly, Finite bias visibility of the electronic Mach-Zehnder interferometer. *Phys. Rev. B* **76**, 161309 (2007).
14. E. Bieri, M. Weiss, O. Göktas, M. Hauser, C. Schönenberger, S. Oberholzer, Finite-bias visibility dependence in an electronic Mach-Zehnder interferometer. *Phys. Rev. B* **79**, 245324 (2009).
15. D. A. Abanin, L. S. Levitov, Quantized transport in graphene *p-n* junctions in a magnetic field. *Science* **317**, 641–643 (2007).
16. J. R. Williams, L. Dicarlo, C. M. Marcus, Quantum Hall effect in a gate-controlled *p-n* junction of graphene. *Science* **317**, 638–641 (2007).
17. A. H. Castro Neto, F. Guinea, N. M. R. Peres, K. S. Novoselov, A. K. Geim The electronic properties of graphene. *Rev. Mod. Phys.* **81**, 109–162 (2009).
18. A. F. Young, C. R. Dean, L. Wang, H. Ren, P. Cadden-Zimansky, K. Watanabe, T. Taniguchi, J. Hone, K. L. Shepard, P. Kim, Spin and valley quantum Hall ferromagnetism in graphene. *Nat. Phys.* **8**, 550–556 (2012).
19. A. A. Zibrov, C. R. Kometter, T. Taniguchi, K. Watanabe, M. P. Zaletel, A. F. Young, Robust nonabelian ground states and continuous quantum phase transitions in a half filled bilayer graphene Landau level. https//arxiv.org/abs/1611.07113 (2016).
20. J. Tworzydlo, I. Snyman, A. R. Akhmerov, C. W. J. Beenakker, Valley-isospin dependence of the quantum Hall effect in a graphene *p-n* junction. *Phys. Rev. B* **76**, 035411 (2007).
21. B. Özyilmaz, P. Jarillo-Herrero, D. Efetov, D. A. Abanin, L. S. Levitov, P. Kim, Electronic transport and quantum Hall effect in bipolar graphene *p-n-p* junctions. *Phys. Rev. Lett.* **99**, 166804 (2007).
22. J. Velasco, G. Liu, W. Bao, C. N. Lau, Electrical transport in high-quality graphene *pnp* junctions. *New J. Phys.* **11**, 095008 (2009).
23. S. Matsuo, S. Takeshita, T. Tanaka, S. Nakaharai, K. Tsukagoshi, T. Moriyama, T. Ono, K. Kobayashi, Edge mixing dynamics in graphene *p-n* junctions in the quantum Hall regime. *Nat. Commun.* **6**, 8066 (2015).
24. T. Machida, S. Morikawa, S. Masubuchi, R. Moriya, M. Arai, K. Watanabe, T. Taniguchi, Edge-channel transport of Dirac fermions in graphene quantum Hall junctions. *J. Phys. Soc. Jpn.* **84**, 121007 (2015).
25. E. Tóvári, P. Makk, M. Liu, P. Rickhaus, Z. Kovács-Krausz, K. Richter, C. Schönenberger, S. Csonka, Gate-controlled conductance enhancement from quantum Hall channels along graphene p-n junctions. *Nanoscale* **8**, 19910–19916 (2016).
26. N. Klimov, S. T. Le, J. Yan, P. Agnihotri, E. Comfort, J. U. Lee, D. B. Newell, C. A. Richte, Edge-state transport in graphene p-n junctions in the quantum Hall regime. *Phys. Rev. B* **92**, 241301 (2015).
27. J. R. Williams, C. M. Marcus, Snake states along graphene *p-n* junctions. *Phys. Rev. Lett.* **107**, 046602 (2011).
28. P. Rickhaus, P. Makk, M. Liu, E. Tóvári, M. Weiss, R. Maurand, K. Richter, C. Schönenberger, Snake trajectories in ultraclean graphene p-n junctions. *Nat. Commun.* **6**, 6470 (2015).
29. T. Taychatanapat, J. You Tan, Y. Yeo, K. Watanabe, T. Taniguchi, B. Özyilmaz, Conductance oscillations induced by ballistic snake states in a graphene heterojunction. *Nat. Commun.* **6**, 6093 (2015).
30. H. Overweg, H. Eggimann, M.-H. Liu, A. Varlet, M. Eich, P. Simonet, Y. Lee, K. Watanabe, T. Taniguchi, K. Richter, V. I. Fal'ko, K. Ensslin, T. Ihn, Oscillating magnetoresistance in graphene p-n junctions at intermediate magnetic fields. *Nano Lett.* **17**, 2852–2857 (2017).
31. M. Kharitonov, Phase diagram for the $\nu = 0$ quantum Hall state in monolayer graphene. *Phys. Rev. B* **85**, 155439 (2012).
32. A. F. Young, J. D. Sanchez-Yamagishi, B. Hunt, S. H. Choi, K. Watanabe, T. Taniguchi, R. C. Ashoori, P. Jarillo-Herrero, Tunable symmetry breaking and helical edge transport in a graphene quantum spin Hall state. *Nature* **505**, 528–532 (2014).
33. L. Wang, I. Meric, P. Y. Yuang, Q. Gao, Y. Gao, H. Tran, T. Taniguchi, K. Watanabe, L. M. Campos, D. A. Muller, J. Guo, P. Kim, J. Hone, K. L. Shepard, C. R. Dean, One-dimensional electrical contact to a two-dimensional material. *Science* **342**, 614–617 (2013).
34. D. T. McClure, Y. Zhang, B. Rosenow, E. M. Levenson-Falk, C. M. Marcus, L. N. Pfeiffer, K. W. West, Edge-state velocity and coherence in a quantum Hall Fabry-Pérot interferometer. *Phys. Rev. Lett.* **103**, 206806 (2009).
35. Y. Zhang, Y.-W. Tan, H. L. Stormer, P. Kim, Experimental observation of the quantum Hall effect and Berry's phase in graphene. *Nature* **438**, 201–204 (2005).

Acknowledgments: We acknowledge the helpful discussions and feedback from A. Kou, B. E. Feldman, D. Nandi, J. I. J. Wang, K. Shain, P. Kim, A. Stern, M. Heiblum, C. Schonenberger, K. Wang, S. H. Wei, S. L. Tomarken, and S. P. Harvey. We also thank G. H. Lee, J. I. Wang, J. Y. Luo, and X. Liu for help with fabrication. **Funding:** This work was primarily supported by the U.S. Department of Energy, Basic Energy Sciences Office, Division of Materials Sciences and Engineering under award DE-SC0001819 (D.S.W., J.D.S.-Y., P.J.-H., and A.Y.). D.S.W. acknowledges partial support from the NSF Graduate Research Fellowship under grant no. DGE1144152. B.I.H. acknowledges support from the STC Center for Integrated Quantum Materials, NSF grant DMR-1231319. K.W. and T.T. acknowledge support from the Elemental Strategy Initiative conducted by the Ministry of Education, Culture, Sports, Science and Technology, Japan and Japan Society for the Promotion of Science KAKENHI grant numbers JP26248061, JP15K21722, and JP25106006. This work was performed in part at the Harvard University Center for Nanoscale Systems, a member of the National Nanotechnology Coordinated Infrastructure Network, which is supported by the NSF under NSF ECCS award no. 1541959. **Author contributions:** D.S.W., T.v.d.S., B.I.H., and A.Y. conceived and designed the experiments. D.S.W. fabricated the devices. D.S.W., T.v.d.S., J.D.S.-Y., and A.Y. performed the experiments. D.S.W., T.v.d.S., J.D.S.-Y., P.J.-H., B.I.H., and A.Y. analyzed the data, developed the models, and wrote the paper. K.W. and T.T. provided the hBN crystals used in the devices. **Competing interests:** The authors declare that they have no competing interests. **Data and materials availability:** All data needed to evaluate the conclusions in the paper are present in the paper and/or the Supplementary Materials. Additional data related to this paper may be requested from the authors.

Submitted 27 February 2017
Accepted 14 July 2017
Published 18 August 2017
10.1126/sciadv.1700600

Citation: D. S. Wei, T. van der Sar, J. D. Sanchez-Yamagishi, K. Watanabe, T. Taniguchi, P. Jarillo-Herrero, B. I. Halperin, A. Yacoby, Mach-Zehnder interferometry using spin- and valley-polarized quantum Hall edge states in graphene. *Sci. Adv.* **3**, e1700600 (2017).

ScienceAdvances

Mach-Zehnder interferometry using spin- and valley-polarized quantum Hall edge states in graphene

Di S. Wei, Toeno van der Sar, Javier D. Sanchez-Yamagishi, Kenji Watanabe, Takashi Taniguchi, Pablo Jarillo-Herrero, Bertrand I. Halperin and Amir Yacoby

Sci Adv **3** (8), e1700600.
DOI: 10.1126/sciadv.1700600